



1 **Observational Constraints Suggest a Smaller Effective Radiative** 2 **Forcing from Aerosol-Cloud Interactions**

3 Chanyoung Park^{1*}, Brian J. Soden¹, Ryan J. Kramer², Tristan S. L'Ecuyer³, Haozhe He⁴

4 1. Rosenstiel School of Marine, Atmospheric, and Earth Science, University of Miami, Miami, FL, USA,

5 2. NOAA/Geophysical Fluid Dynamics Laboratory, Princeton, NJ, USA,

6 3. University of Wisconsin–Madison, Madison, WI, USA,

7 4. High Meadows Environmental Institute, Princeton University, Princeton, NJ, USA.

8 *Corresponding author: Chanyoung Park (chanyoung.park@miami.edu)

9

10 **Abstract**

11 The effective radiative forcing due to aerosol-cloud interactions (ERF_{aci}) is difficult to quantify,
12 leading to large uncertainties in model projections of historical forcing and climate sensitivity.
13 In this study, satellite observations and reanalysis data are used to examine the low-level cloud
14 radiative responses to aerosols. While some studies it is assumed that the activation rate of
15 cloud droplet number concentration (N_a) in response to variations in sulfate aerosols (SO_4) or
16 the aerosol index (AI) has a one-to-one relationship in the estimation of ERF_{aci}, we find this
17 assumption to be incorrect, and demonstrate that explicitly accounting for the activation rate is
18 crucial for accurate ERF_{aci} estimation. This is corroborated through a “perfect-model” cross
19 validation using state-of-the-art climate models, which compares our estimates with the “true”
20 ERF_{aci}. Our results suggest a smaller and less uncertain value of the global ERF_{aci} than
21 previous studies ($-0.39 \pm 0.29 \text{ W m}^{-2}$ for SO_4 and $-0.24 \pm 0.18 \text{ W m}^{-2}$ for AI, 90% confidence),
22 indicating that ERF_{aci} may be less impactful than previously thought. Our results are also
23 consistent with observationally constrained estimates of total cloud feedback and “top-down”
24 estimates that models with weaker ERF_{aci} better match the observed hemispheric warming
25 asymmetry over the historical period.

26

27 **1. Introduction**

28 Anthropogenic aerosols impact the Earth's radiation balance at the top of the atmosphere and
29 alter cloud properties over the industrial era (Boucher et al., 2013; Raghuraman et al., 2021;
30 Kramer et al., 2021). They directly alter the radiation budget by scattering and absorbing solar
31 radiation and indirectly influence it by serving as cloud condensation nuclei (CCN), which



32 modifies cloud properties and can extend their duration. This increase in aerosol concentration
33 leads to smaller cloud droplets and higher cloud albedos, known as the “Twomey effect” (e.g.,
34 Twomey, 1977), enhancing the radiative forcing due to aerosol-cloud interactions (RFaci).
35 Additionally, aerosols affect cloud microphysical properties (e.g., Albrecht, 1989; Pincus and
36 Baker, 1994), such as reducing precipitation, which increases cloud liquid water path (LWP),
37 lifetime, and fraction, a process termed cloud adjustment (CA). Thus, together, RFaci and CA
38 are intrinsically interconnected through the cloud droplets (Mülmenstädt and Feingold, 2018),
39 and constitute the ERFaci, which is highly uncertain and often larger than the direct radiative
40 impact of aerosols (Forster et al., 2007; Zelinka et al., 2014; Smith et al., 2020a).

41

42 Estimating the ERFaci, especially in low-level clouds which are the dominant contributor of
43 aerosol-cloud interactions to ERFaci (Christensen et al., 2016; Bellouin et al., 2020; Forster et
44 al., 2021), is critical for accurately identifying cloud feedback mechanisms and determining
45 climate sensitivity (Rosenfeld, 2006; Boucher et al., 2013; Sherwood et al., 2020). Our study
46 provides quantitative insights into the ERFaci using both satellite observations and reanalysis
47 data. A key component of our analysis is the activation rate, which serves as a metric for
48 assessing the actual impact of aerosols on cloud droplet number concentrations. The
49 conventional assumption is that the activation rate has a one-to-one relationship when aerosols
50 convert into cloud droplets and is typically not explicitly incorporated into the estimation
51 process of ERFaci. Our results suggest the importance of considering the activation rate when
52 evaluating the interactions between aerosols and clouds. To evaluate the robustness of our
53 results, we conduct a “perfect-model” cross validation using Coupled Model Intercomparison
54 Project Phase 6 (CMIP6) simulations. This form of cross-validation is widely used in statistics
55 and machine learning to assess the generalizability of predictive models and prevent overfitting
56 (Wenzel et al., 2016; Knutti et al., 2017; Brunner et al., 2020). Through this approach we
57 demonstrate that explicitly including the activation rate is essential to improving the accuracy
58 of ERFaci estimates. Although open questions remain, the cross-validation clearly
59 demonstrates the improved predictive skill of our model and thus increases the confidence of
60 our estimates of ERFaci.

61

62 In the main text, our analysis primarily focuses on SO₄ as an aerosol proxy, recognized as a
63 major contributor among other aerosol types such as black carbon, organic carbon, sea salt, and
64 dust (Charlson et al., 1992; McCoy et al., 2018). However, results derived from the Aerosol



65 Index (AI), a more generalized aerosol metric (e.g. Douglas and L'Ecuyer 2019, 2020), also
66 show a high degree of consistency.

67

68 **2. Results**

69 **2.1 Activation Rate**

70 Some approaches to estimate the ERF_{aci} with aerosol concentrations have operated under a
71 key assumption: the natural logarithm of aerosol concentration correlates proportionally with
72 the natural logarithm of cloud droplet number concentration (Boucher and Lohmann, 1995;
73 Wall et al., 2022, 2023). This ratio, commonly referred to as the activation rate, quantifies the
74 efficiency with which aerosol particles convert into cloud droplets. The hypothesized cause-
75 effect relationship between aerosols and clouds is important to understand and to be dealt in
76 the process of aerosol-cloud interactions, as it involves an increase in CCN leading to an
77 increase in N_d , which subsequently influences cloud properties. To verify the key assumption,
78 we performed a linear regression. As illustrated in Fig. 1, the regression coefficients between
79 $\ln(N_d)$ and $\ln(SO_4)$ were calculated. Our results show that, in most regions, these coefficients
80 are positive but less than 1. This indicates that while there is a proportional relationship, it is
81 not a one-to-one increase; rather, the activation rate varies across different geographic locations.
82 Regions with shallow cumulus clouds, such as the central Pacific, show a notably weaker
83 $\partial \ln(N_d) / \partial \ln(SO_4)$ coefficient, while areas with stratocumulus clouds, like those off the coasts
84 of continents, display a relatively stronger positive regression with significant correlation
85 coefficient (Fig. 1). Repeating our analysis using $\partial \ln(N_d) / \partial \ln(AI)$ also yields results consistent
86 with those for $\ln(SO_4)$, emphasizing the necessity of addressing this assumption within the
87 ERF_{aci} estimation process (Fig. A1). The relatively low correlation coefficients observed for
88 $\partial \ln(N_d) / \partial \ln(AI)$ may be attributed to the use of column-integrated quantities, AI from MODIS,
89 which do not account for the vertical structure of aerosols. Consequently, they may not
90 accurately represent aerosol concentrations at cloud base height. In contrast, the use of SO_4
91 concentration at 925 hPa in the analysis provides a more precise representation of CCN
92 concentrations near the cloud base (Painemal et al., 2017). This leads to a higher linearity
93 between SO_4 and N_d , establishing SO_4 a more relevant indicator for evaluating the interactions
94 between aerosols and low-level cloud formation (Fig. 1 vs Fig. A1).

95



96 2.2 Observationally Constrained ERF_{aci}

97 To isolate the contributions of different environmental factors to the low cloud radiative effect,
98 we first have employed a cloud controlling factor (CCF) analysis (Scott et al., 2020; Wall et
99 al., 2022) with a particular focus on elucidating the relationship between aerosol concentrations
100 and the low cloud radiative effect. This relationship is known as a susceptibility and constitutes
101 one of the key components in the estimation of ERF_{aci}. Our implementation of the CCF
102 analysis basically follows the method described by Wall et al. (2022) (See more details in
103 Appendix A).

104

105 We now proceed to estimate the observationally constrained ERF_{aci} (ERF_{aci_obs}),
106 considering two scenarios: one with and the other without the inclusion of the activation rate.
107 The basic form of ERF_{aci_obs} following Wall et al. (2022), where the activation rate is not
108 explicitly included, can be expressed as follows:

109

$$110 \quad \text{ERF}_{\text{aci_obs}} \approx \sum_{k=1}^{10} \left(\frac{\partial \text{CRE}_{\text{lcd}}}{\partial \ln(Y)} \right)_k W_k \times \Delta \ln(Y), \quad (1)$$

111

112 where CRE_{lcd} represents the cloud radiative effect from low-level clouds, Y represents either
113 SO₄ or AI, and W_k represents the fraction of LWP in state k ($W_k = \frac{\text{number in LWP state } k}{\text{total number}}$). The
114 right-hand-side of the equation consists of two main parts: one is the susceptibility of the low-
115 cloud radiative effect to variations in aerosol concentrations, which can be derived from CCF
116 analysis using observations and the other one is the changes in aerosol concentrations from
117 pre-industrial (PI) to present-day (PD). Due to the lack of observational data on PI aerosol
118 concentrations, we employ the outputs of CMIP6 historical experiments. As expected, changes
119 in SO₄ concentrations exhibit distinctive spatial patterns characterized by interhemispheric
120 asymmetry, with particularly large values in proximity to major industrial regions on the
121 Eurasian and North American continents (Fig. 2a).

122

123 In light of Fig. 1, the basic form of ERF_{aci_obs} in equation (1) can be expanded to incorporate
124 the influence of the activation rate by accounting for the interactions between aerosols and
125 cloud droplet formation. This modified equation can be expressed as follows:

126



127
$$\text{ERFaci}_{\text{obs}} \approx \sum_{k=1}^{10} \left(\frac{\partial \text{CRE}_{\text{lclld}}}{\partial \ln(N_d)} \times \frac{\partial \ln(N_d)}{\partial \ln(Y)} \right)_k W_k \times \Delta \ln(Y), \quad (2)$$

128

129 where the low cloud susceptibility is now the product of two terms: The susceptibility of low
130 cloud CRE to N_d and the activation rate of Y to N_d .

131

132 Our analysis reveals pronounced differences in susceptibility in how low cloud radiative effects
133 respond to variations in aerosol concentrations across the globe depending on whether
134 activation rate is considered or not. The inclusion of the activation rate in our analysis
135 significantly diminishes the sensitivity of clouds to aerosols (Fig. 2b vs Fig. 2c). Noticeable
136 decreases in susceptibility are captured in mid-latitudes and in subtropical regions where low
137 clouds are dominant. This also indicates that the $\partial \ln(\text{CRE}_{\text{lclld}})/\partial \ln(\text{SO}_4)$ correlation without
138 activation rate is partially attributable to factors other than the N_d -mediated mechanism (Wood
139 et al., 2012; Gryspeerdt et al., 2016; Gryspeerdt et al., 2019).

140

141 Both methods of estimating $\text{ERFaci}_{\text{obs}}$ show that an increase in aerosol concentration
142 correlates with a negative cloud radiative adjustment that is especially prevalent in areas
143 dominated by low clouds (Fig. 2d,e). However, due to the reduced susceptibility, the estimated
144 $\text{ERFaci}_{\text{obs}}$ is significantly smaller when activation is explicitly accounted for (Fig. 2e) than
145 when it is not (Fig. 2d). The global $\text{ERFaci}_{\text{obs}}$ is ~50% smaller with activation (-0.39 W m^{-2})
146 than without (-0.79 W m^{-2}). Similar results are obtained if one uses AI instead of SO_4 as the
147 measure of aerosol concentration (Fig. A2d,e). These results highlight the sensitivity of this
148 approach to explicit consideration of the activation rate.

149

150 **2.3 Perfect-Model Cross Validation**

151 In this section, we perform a “perfect-model” cross validation exclusively using CMIP6
152 simulations to assess which of the two approaches—considering activation rate or not—is more
153 accurate. Specifically, each model from single-forcing (aerosol-only) experiments is
154 sequentially treated as the “truth” with its ERFaci considered the “true” value. Meanwhile, the
155 same model from historical simulations, assumed to be a pseudo-observation, estimates ERFaci
156 for comparison with the “true” ERFaci . The resulting root mean-square error (RMSE) provides
157 a quantitative measure of the accuracy of the ERFaci estimates.



158

159 As an initial step in the “perfect-model” test, single-forcing (aerosol-only) CMIP6 simulations
160 are used to establish the true ERFaci for each model, referred to as ERFaci_{true}, which
161 provides a benchmark for assessing the accuracy of the ERFaci estimated from the monthly
162 outputs of CMIP6 historical experiments using equations (1) and (2), where the model is treated
163 as a pseudo-observation and the estimate is referred to as ERFaci_{est}. Because the number of
164 CMIP6 models that provide single-forcing (aerosol-only) simulations for ERFaci_{true} is
165 limited, we also explore another technique for estimating ERFaci introduced by Soden and
166 Chung (2017; referred to as ERFaci_{SC17}) that has been previously shown to agree well with
167 ERFaci_{true} (Chung and Soden, 2017). For more details on the estimation of these three
168 different ERFaci using CMIP6 model outputs, please refer to Appendix A. A comparison, for
169 the “perfect-model” test, of ERFaci_{est} with both ERFaci_{true} and ERFaci_{SC17} is provided
170 below.

171

172 Fig. 3 illustrates the correlation between ERFaci_{true} and two alternative approaches derived
173 from CMIP6 model output. The estimates of ERFaci_{est} that omit the activation rate fail to
174 replicate the “true” ERFaci values accurately, with RMSE of 0.68 W m⁻² and bias of 0.56 W m⁻².
175 Conversely, incorporating an explicit activation rate into the ERFaci estimates provides
176 significantly better agreement with ERFaci_{true}, reducing both the RMSE and bias by around
177 40% (Fig. 3a).

178

179 ERFaci_{SC17} exhibits the best agreement with ERFaci_{true}, with significantly smaller RMSE
180 (0.14 W m⁻²) and bias (0.1 W m⁻²) (Fig. 3b). This consistency allows us to expand the sample
181 size of CMIP6 models, with which we can evaluate ERFaci_{est} by using ERFaci_{SC17} as a
182 surrogate for ERFaci_{true} (Fig. 3c). This expanded cross-validation once again highlights the
183 importance of including the activation rate in ERFaci estimates, as it reduces both the RMSE
184 and bias in ERFaci_{est} by around 45%. Substituting AI for SO₄ in the calculation of ERFaci_{est}
185 yields similar results, which reduces RMSE more than 40%, emphasizing the importance of
186 explicitly including activation rate (Fig. A3). Our “perfect-model” cross validation analysis
187 with idealized model experiments from CMIP6 leads us to conclude that the inclusion of the
188 activation rate is essential for accurate estimates of ERFaci.

189



190 **2.4 Comparison with previous ERFaci estimates**

191 Now, we compare our observationally constrained estimates of ERFaci_obs with those
192 previously estimated. Our global estimates with inclusion of activation rate yield an ERFaci of
193 $-0.39 \pm 0.29 \text{ W m}^{-2}$ for SO₄ and $-0.24 \pm 0.18 \text{ W m}^{-2}$ for AI (Fig. 4). These values are at the
194 lower bound when compared with ERFaci values reported in the Sixth Assessment Report of
195 the Intergovernmental Panel on Climate Change (IPCC; Forster et al., 2021) as well as the
196 values proposed by the World Climate Research Program (WCRP; Bellouin et al., 2020).
197 However, it is worth noting that, as the ERFaci from WCRP has a highly skewed distribution
198 with its highest probability occurring around -0.4 W m^{-2} , which is entirely consistent with our
199 observational estimates (Fig. 4). Given the multiple lines of evidence introduced by the WCRP,
200 which employs a process-oriented approach to bound ERFaci, our estimates offer further
201 evidence to support estimates on the lower end of their range. Furthermore, these constrained
202 ERFaci_obs are also consistent with the “top-down” estimates provided by Wang et al. (2021),
203 which demonstrate that models exhibiting weaker ERFaci are more in line with the observed
204 variations in global mean surface temperature as well as hemispheric warming asymmetry
205 during the historical period.

206

207 As we emphasized the significant impact of including the activation rate in the ERFaci
208 estimation process, with this inclusion, the ERFaci_obs values are approximately one-half for
209 SO₄ and one-fifth for AI of those estimated without considering the activation rate, respectively
210 ($-0.79 \pm 0.28 \text{ W m}^{-2}$ for SO₄ and $-1.14 \pm 0.29 \text{ W m}^{-2}$ for AI).

211

212 **2.5 Implications for Cloud Feedback**

213 Our observational estimate of ERFaci is on the lower end compared to previous estimates. This
214 finding also has implications for our understanding of cloud feedback mechanisms. Following
215 Wang et al. (2021), we compare the CMIP6 historical simulations of ERFaci across different
216 climate models with their corresponding values of total cloud feedback, which are derived from
217 the regression slope of total cloud radiative response to global-mean temperature anomalies
218 from the abrupt-4xCO₂ experiment (Fig. 5). For this analysis, we use the ERFaci_SC17 since
219 it ensures the widest possible selection of climate models (Table A1). Among the models we
220 assessed, we identified a subset of 15 that we termed 'GOOD HIST' models (Appendix A).
221 These models are characterized by their small discrepancies in simulating global-mean
222 historical surface warming when compared to the GISTEMP observational data, indicating a



223 higher reliability in their historical climate simulations. Within this subset, a strong negative
224 correlation ($r = -0.85$) exists between ERFaci_SC17 and the total cloud feedback, which is
225 much more pronounced than in the remaining models ($r = -0.31$). The strong correlation in the
226 'GOOD HIST' models highlights the compensation that occurs between historical aerosol
227 forcing and cloud feedback in order for models to reproduce the observed historical global-
228 mean temperature.

229

230 Also shown are the probability density functions for the observation-based estimates of
231 ERFaci_obs, taking into account the activation rate, and utilizing both SO₄ and the AI.
232 Alongside, we also consider the observationally constrained estimates of total cloud feedback,
233 which a recent study (Ceppi and Nowack, 2021) has quantified at $0.43 \pm 0.35 \text{ W m}^{-2} \text{ K}^{-1}$ (90%
234 confidence). These distributions help illustrate that our constraints on ERFaci fall within the
235 realistic bounds of total cloud feedback strength. The best estimates, which show the highest
236 probability (indicated by stars), also align with those from the 'GOOD HIST' models and
237 support the validity of our constraints.

238

239 **3. Conclusion**

240 Our study offers critical insights into the quantification of ERFaci, a topic that remains a
241 significant source of uncertainty in understanding climate sensitivity. By integrating both
242 satellite observations and reanalysis data with a focus on the activation rate of cloud droplet
243 number concentration in response to aerosol variations, we provide a more sophisticated
244 understanding of the impact of aerosols on low-level clouds. Our findings, validated through a
245 “perfect-model” cross validation using CMIP6 model simulations, reveal a lower global
246 ERFaci estimate, suggesting that the influence of aerosols, particularly with SO₄, on climate
247 forcing may be less substantial than previously assumed.

248

249 **Appendix A: Methods**

250 **A1 Observation and Reanalysis Data**

251 **A1.1 CERES**

252 In this study, we analyze observational datasets characterized by their monthly temporal
253 resolution and their geographical coverage extending from 50°S to 50°N, with a particular
254 focus on oceanic regions due to unreliable retrieval over land (Jia et al., 2019; Gryspeerdt et



255 al., 2022; Jia and Quaas, 2023). The dataset spans from January 2003 through December 2019
256 and all data fields were interpolated onto a $2.5^\circ \times 2.5^\circ$ grid.

257

258 Our analysis employs monthly gridded satellite observations from the CERES FluxByCldTyp
259 Edition 4.1 dataset, focusing on a combined analysis of cloud fraction and top-of-atmosphere
260 radiative flux, segmented by cloud optical depth and cloud top pressure (CTP). We categorize
261 clouds into low (CTP > 680 hPa) and non-low clouds (CTP \leq 680 hPa) based on their CTP
262 values. Due to the passive retrieval mechanisms of satellite instruments, the detection of low-
263 level clouds is notably challenged by the obscuration from upper-level clouds. This limitation
264 highlights the importance of accurately estimating the fraction of non-obscured or non-
265 overlapped low-level clouds (Scott et al., 2020). To address this, we define the non-obscured
266 low-cloud fraction as following equation:

267
$$L_n = \frac{L}{1 - U}, \quad (A1)$$

268 where L and U represent the low and non-low cloud fraction retrieved by the satellite, and L_n
269 denotes the total low-level cloud fraction relative to the area of each grid box that is not
270 obscured by upper-level clouds. With this relationship, we can extend its application to the
271 cloud radiative effect (CRE) attributable to non-obscured low-level clouds (CRE_lclld). Further
272 details regarding this equation can be found in the work of Scott et al. (2020).

273

274 **A1.2 MERRA-2 reanalysis**

275 We also use monthly meteorological fields for cloud controlling factor analysis and sulfate
276 aerosol mass concentrations at 925 hPa derived from the Modern-Era Retrospective analysis
277 for Research and Applications, Version 2 (MERRA-2) reanalysis (Randles et al., 2017; Gelaro
278 et al., 2017). MERRA-2 integrates observations with global model simulations to provide
279 estimates of atmospheric conditions. Specifically for sulfate aerosols, it employs bias-corrected
280 observations of total aerosol optical depth in conjunction with a comprehensive model
281 addressing the emissions, removal processes, and chemistry of sulfate and its precursor gases.
282 The assimilation process adjusts for aerosol hydration in humid conditions and excludes cloud-
283 adjacent pixels to mitigate retrieval bias. A notable constraint of these data is that, while the
284 total aerosol optical depth is observationally constrained, the distribution and vertical profiles
285 of aerosol species are model-derived. Nevertheless, the sulfate concentration estimates exhibit
286 a strong correlation with independent satellite measurements of cloud droplet number



287 concentration (McCoy et al., 2018).

288

289 **A1.3 MODIS**

290 We employ the aerosol index (AI) as an alternative proxy for aerosol concentration from the
291 Moderate Resolution Imaging Spectroradiometer (MODIS) on both the Aqua and Terra
292 satellites (datasets MYD08_M and MOD08_M, respectively). These two are combined to
293 enhance the robustness of our analysis. The AI is derived from the product of the Angstrom
294 exponent and the aerosol optical depth (AOD) at 550 nm. The Angstrom exponent itself is
295 derived from the wavelength dependency of the AOD, measured at 550 nm and 870 nm,
296 providing insight into the size distribution of aerosols (i.e. smaller Angstrom exponent suggests
297 larger particles). Notably, AI has demonstrated a more robust correlation with CCN compared
298 to the use of AOD alone (Stier, 2016; Gryspeerdt et al., 2017; Hasekamp et al., 2019).

299

300 To calculate N_d based on the adiabatic approximation, we use daily gridded N_d estimates from
301 MODIS (Gryspeerdt et al., 2022) and combine the data from the Aqua and Terra satellites. The
302 retrievals at 3.7 μm , known to yield more accurate cloud droplet effective radius (r_e)
303 measurements under inhomogeneous conditions, are employed (Zhang and Platnick, 2011). N_d
304 measurements may be subject to biases under specific conditions, such as when the cloud
305 droplet effective radius is significantly small, when the cloud visible optical thickness is low,
306 or when three-dimensional radiative transfer effects impact the observed radiances. To enhance
307 the accuracy and reliability of our N_d retrievals, we implement a rigorous sampling strategy
308 (“BR17 sampling method” in Gryspeerdt et al., 2022). This introduced by Bennartz and Rausch
309 (2017) demonstrates the highest correlation with aircraft data.

310

311 For LWP, MODIS MCD06COSP dataset version 6.2.0 (Pincus et al., 2023) is used. This dataset
312 represents a combined product derived from both the Aqua and Terra satellites. To accurately
313 estimate the aerosol indirect effect, it is essential to control variations in LWP, in line with the
314 foundational assumption of the Twomey effect. In our analysis, we achieve this by categorizing
315 LWP observations into ten equal bins, each covering a range of 30 g cm^{-2} , up to a maximum of
316 300 g cm^{-2} . This categorization is based on the finding that over 99% of our observations do
317 not exceed 300 g cm^{-2} , thus allowing us to maintain LWP within a controlled and effectively
318 constant range across our dataset.

319



320 **A1.4 GISTEMP**

321 The global surface temperature observations used in our analysis are sourced from the GISS
322 Surface Temperature Analysis (GISTEMP v4) (Lenssen et al., 2019). We evaluate how well the
323 models simulate the global-mean historical surface warming by the GOOD HIST index: the
324 absolute difference in global-mean historical warming between CMIP6 models and GISTEMP
325 data (Table A1). The historical warming is defined as the averaged surface temperature in
326 1990–2014 minus that in 1880–1909. So, the models that are good at simulating the historical
327 warming have a small GOOD HIST index.

328

329 **A2 CMIP6 Data**

330 Due to the unavailability of direct observational records for pre-industrial aerosol emissions,
331 we rely on the outputs from historical simulations with realistic emissions of greenhouse gases,
332 aerosols, and aerosol precursor gases conducted by CMIP6 models to estimate changes in
333 aerosol concentration ($\Delta \ln(Y)$, where Y represents either SO_4 or AI). The pre-industrial (PI)
334 period was defined as the years 1850 to 1899, and the present-day (PD) period was set from
335 1965 to 2014, each spanning 50 years to remove interannual variability. In the analysis, 13
336 models are used for $\Delta \ln(SO_4)$ and 9 models for $\Delta \ln(AI)$, all models of which are among the
337 21 models that provide $ERFaci_true$. The specific models used in our analysis are listed in
338 Table A1. It is important to note that, for the CMIP6 models, the emission concentrations of
339 sulfur dioxide, a precursor to SO_4 , are specified from the Community Emission Data Set
340 (CEDS; Hoesly et al., 2018), and thus the projected changes in $\Delta \ln(SO_4)$ are highly consistent
341 across models. The specified decadal trends in regional sulfate in the models are also consistent
342 with surface observations (Aas et al., 2019).

343

344 To evaluate our observationally constrained estimate of the $ERFaci$ ($ERFaci_obs$), we
345 employed 21 distinct models conducting single-forcing (aerosol-only) experiments
346 ($ERFaci_true$). These models are from the Radiative Forcing Model Intercomparison Project
347 (RFMIP; Pincus et al., 2016), specifically Tier 1 piClim-control and piClim-aer experiments
348 with prescribed sea surface temperatures (SST) and sea ice derived from a climatology of pre-
349 industrial conditions. These simulations are run for 30 years, incorporating realistic aerosol
350 emissions in 1850 and 2014 to represent PI and PD conditions, respectively. This ensures an
351 accurate estimation of the true baseline of $ERFaci$ resulting solely from aerosol-cloud
352 interactions. We use 30-year time periods for the PI and the PD scenario to evaluate $ERFaci$.



353 Consequently, the ERF_{aci} derived from these experiments is referred to as ERF_{aci_true}.

354

355 **A3 Cloud Controlling Factor Analysis**

356 To improve our understanding of the low cloud radiative effect, we have employed a cloud
357 controlling factor (CCF) analysis (Scott et al., 2020; Wall et al., 2022). This approach allows
358 us to constrain the physical factors influencing low cloud properties and their subsequent
359 radiative impacts. The analysis considers a set of controlling factors that are known to be
360 significant drivers of low cloud behavior, which can be expressed as follows:

361

$$362 \quad \text{CRE_lcl}' \approx \sum_{i=1}^7 \frac{\partial \text{CRE_lcl}}{\partial X_i} \times X_i', \quad (\text{A2})$$

363

364 where CRE_{lcl} represents the cloud radiative effect from low-level clouds and the factors (X_i)
365 included in our analysis are 1) sea surface temperatures, 2) estimated inversion strength, 3)
366 horizontal surface temperature advection, 4) relative humidity at 700 hPa, 5) vertical velocity
367 at 700 hPa, and 6) near-surface wind speed. These parameters represent a combination of
368 thermodynamic and dynamic influences that are critical in dictating low cloud formation and
369 persistence (Scott et al., 2020). In addition to these standard meteorological variables, we
370 introduce 7) aerosol concentrations as additional controlling factors (Wall et al., 2022).
371 Specifically, we consider the natural logarithm of sulfate aerosol mass concentrations at 925
372 hPa, $\ln(\text{SO}_4)$. In our analysis, we opt to use data from the 925 hPa atmospheric level instead of
373 surface-level measurements. This decision is based on the understanding that conditions at 925
374 hPa provide a more accurate reflection of CCN concentrations near the cloud base (Painemal
375 et al., 2017). This altitude is often closer to the actual height at which low-level clouds form,
376 making it a more relevant indicator for assessing aerosol-cloud interactions. We also consider
377 the natural logarithm of the aerosol index, $\ln(\text{AI})$ as a metric of the aerosol concentration cloud
378 controlling factor. Note that, as highlighted in the main text, since AI provides column-
379 integrated quantities and does not account for the vertical profile, it may not accurately capture
380 aerosol concentrations in low-level clouds, which are the focus of our study.

381

382 For each grid point, we employ ordinary least-squares multilinear regression to model
383 CRE_{lcl}' against anomalies in the seven cloud controlling factors. The regression coefficients,
384 $\partial \text{CRE_lcl} / \partial \ln(\text{SO}_4)$ and $\partial \text{CRE_lcl} / \partial \ln(\text{AI})$, quantify the sensitivity of low-level cloud



385 radiative effect anomalies ($CRE_lcl d'$) to local anomalies in $\ln(SO_4)$ or $\ln(AI)$, respectively.

386

387 **A4 Estimating ERFaci using CMIP6 model outputs**

388 **A4.1 Estimating ERFaci_true**

389 The ERFaci_true is calculated for PD minus PI conditions from aerosol-only, fixed-SST
390 experiments as,

391

$$392 \quad \text{ERFaci_true} = \Delta \text{CRE_lcl d}, \quad (\text{A3})$$

393

394 where the low-level cloud radiative effect ($\Delta \text{CRE_lcl d}$) is determined by using cloud
395 classification method introduced in Webb et al. (2006) and Soden and Vecchi (2011).

396

397 **A4.2 Estimating ERFaci_SC17**

398 This method partitions the low-level cloud radiative response observed in historical
399 experiments into two components: one is a temperature-mediated component (i.e., cloud
400 feedback) attributable to changes in the global-mean surface temperature and the other to
401 aerosol-cloud interactions. The temperature-mediated component is estimated by multiplying
402 the global-mean temperature anomaly by the low-level cloud feedback, derived from the
403 1pctCO₂ scenario ($\alpha_{1\text{pctCO}_2}$), which is calculated as the low-level cloud radiative response
404 normalized by the corresponding global-mean surface warming. This estimate of ERFaci is
405 then obtained by subtracting this temperature-driven component from the low-level cloud
406 radiative response, thus focusing solely on the impact of aerosol-cloud interactions.

407

$$408 \quad \text{ERFaci}_{\text{SC17}} = \Delta \text{CRE_lcl d} - \alpha_{1\text{pctCO}_2} \cdot \Delta \bar{T}_s. \quad (\text{A4})$$

409

410 Because this method uses outputs from historical and 1pctCO₂ simulations, it allows a much
411 larger sample size of models to evaluate the two different versions of ERFaci_est.

412

413 **A4.3 Estimating ERFaci_est**

414 To estimate ERFaci_est, derived exclusively from CMIP6 model outputs calculated using
415 equations (1) and (2) from the main text, we use monthly anomalies spanning from 2000 to
416 2014 in historical experiments for susceptibility calculation, after removing trends and
417 climatological seasonality. We adhere to the same timeframe for aerosol concentration changes



418 as described in the main text. Additionally, given the challenges associated with deriving cloud-
419 top cloud droplet number concentrations (N_d) directly from CMIP6 model outputs, we adopt
420 an alternative approach, which is the maximum N_d within a vertical atmospheric column
421 (Saponaro et al., 2020; Jia and Quaas, 2023). Owing to the limited availability of models for
422 CCF analysis and LWP binning, both are not explicitly employed in the estimation process of
423 ERF_{faci_est} . Instead, we assess the impact of including or excluding CCF analysis and LWP
424 binning on ERF_{faci_obs} to elucidate their influence on the estimation of ERF_{faci_est} . The
425 simplified version of equations (1) and (2), which do not account for CCF analysis and LWP
426 binning, are presented below:

427

$$428 \quad ERF_{faci_obs} \approx \frac{\partial CRE_{lclcd}}{\partial \ln(Y)} \times \Delta \ln(Y), \quad (A5)$$

429 (without CCF analysis, LWP binning, and activation rate)

430

$$431 \quad ERF_{faci_obs} \approx \left(\frac{\partial CRE_{lclcd}}{\partial \ln(N_d)} \times \frac{\partial \ln(N_d)}{\partial \ln(Y)} \right) \times \Delta \ln(Y), \quad (A6)$$

432 (without CCF analysis and LWP binning but with activation rate)

433

434 When applying these equations to estimate ERF_{faci_obs} , we obtain best estimates of global-
435 mean ERF_{faci_obs} (without activation rate) of -1.46 for SO_4 and -1.74 for AI, and global-mean
436 ERF_{faci_obs} (with activation rate) of -0.61 for SO_4 and -0.34 for AI. These values are 1.85,
437 1.53, 1.56, and 1.42 times larger, respectively, than those obtained when considering CCF
438 analysis and LWP binning. In other words, by dividing model-driven ERF_{faci} estimates by these
439 factors, we can approximate its value under scenarios that include CCF analysis and LWP
440 binning (ERF_{faci_est}). These outcomes are employed in Fig. 3 and Fig. A3.

441

442 **A5 Radiative Kernel Method**

443 Originally developed by Soden et al. (2008) to facilitate the analysis of radiative feedbacks,
444 “radiative kernels” describe the differential response of radiative fluxes to incremental changes
445 in the radiative state variables (e.g., clouds, temperature, water vapor, albedo). In this study, we
446 employed radiative kernel techniques derived from the HadGEM3-GA7.1 model (Smith et al.,
447 2020b) for all CMIP6 model analysis to isolate the genuine cloud radiative effect without
448 interference from cloud masking effects.

449

450 **A6 Estimating Global-Mean ERF_{faci_obs}**



451 Given that our observation data cover the domain extending from 50°S to 50°N over the ocean,
452 it is imperative to extrapolate global ERFaci values for comparison with the observation-based
453 estimates reported in the IPCC Sixth Assessment Report. Our estimate of the ERFaci_obs spans
454 a near-global domain, encompassing almost 60% of the Earth's surface. This notably includes
455 vast stretches of the remote oceans. Although our estimate does not account for polar oceans,
456 their exclusion is unlikely to significantly skew our results. These regions contribute minimally
457 to the global ERFaci because of their limited surface area. Given these considerations, we
458 believe that our near-global estimate can serve as a reliable proxy for the true global average.
459 This assumption is supported by the result from CMIP6 models (Fig. A4). To bridge the gap
460 between global and domain-specific averages, using 21 CMIP6 climate models in single-
461 forcing experiments (ERFaci_true), we employ a scalar, γ , representing the ratio of the multi-
462 model mean of global-average ERFaci_true to the multi-model mean of domain-average
463 ERFaci_true. We ascertain γ 's value at 0.69 with 0.92 correlation coefficient, enabling the
464 calibration of our domain-specific ERFaci estimates to more accurately reflect a global scale.
465 This calibration is achieved through the following equation:

466

$$467 \quad \text{ERFaci}_{\text{obs, global}} = \gamma \times \text{ERFaci}_{\text{obs, domain}}, \quad (\text{A7})$$

468

469 In ensuring the consistency of our estimates, we adjust the IPCC Sixth Assessment Report's
470 estimate of ERFaci, which uses 2014 as the present-day reference year and 1750 as the
471 preindustrial reference year. The IPCC's initial global estimate for ERFaci between 2014 and
472 1750 is $-1.0 \pm 0.7 \text{ W m}^{-2}$. To make this preindustrial reference period consistent with our
473 analysis, we subtract the estimated ERFaci of -0.07 W m^{-2} between 1850 and 1750 from the
474 IPCC's value (Dentener et al., 2021). This adjustment yields an estimate based solely on
475 observational evidence, with a 90% CI of $-0.93 \pm 0.7 \text{ W m}^{-2}$ (Wall et al., 2022).

476

477 **A7 Uncertainty**

478 The uncertainty in ERFaci_obs, in the case where the activation rate is not considered, is
479 attributed to uncertainties in the susceptibility, the regression coefficient for $\partial\text{CRE}_{\text{lcd}}/\partial\ln(Y)$,
480 and in the model estimates of $\Delta\ln(Y)$. Conversely, when considering the activation rate,
481 the uncertainty in ERFaci_obs stems from uncertainties in the regression coefficients for
482 $\partial\text{CRE}_{\text{lcd}}/\partial\ln(N_d)$ and $\partial\ln(N_d)/\partial\ln(Y)$, as well as from uncertainties in the model
483 predictions of $\Delta\ln(Y)$.



484

485 To quantify the uncertainty derived from regression coefficients, at each grid box a 90%
 486 confidence interval of the susceptibility is given by

$$487 \quad \delta = t\sqrt{\mathbf{C}_{ii}} \sqrt{\frac{N_{\text{nom}}}{N_{\text{eff}}}} \text{ (without activation rate),} \quad (\text{A8})$$

$$488 \quad \delta = t\sqrt{\Delta\mathbf{x}^T\mathbf{C}\Delta\mathbf{x}} \sqrt{\frac{N_{\text{nom}}}{N_{\text{eff}}}} \text{ (with activation rate),} \quad (\text{A9})$$

489 where t is the critical value of the Student's t -test at the 95% significance level with $N_{\text{eff}} - 7$
 490 degrees of freedom (Von Storch and Zwiers, 1999), \mathbf{C} is the variance–covariance matrix of
 491 regression coefficients hence \mathbf{C}_{ii} represents the diagonal components of the \mathbf{C} , $N_{\text{nom}}/N_{\text{eff}}$ is
 492 the ratio of the nominal to effective number of monthly values of CRE_lcl'd', and $\Delta\mathbf{x}$ is the
 493 regression coefficient for $\partial\ln(N_d)/\partial\ln(Y)$. \mathbf{C} is formulated as $\mathbf{C} = \hat{\sigma}^2(\mathbf{X}^T\mathbf{X})^{-1}$, where \mathbf{X} is
 494 the data matrix with columns composed of detrended monthly anomalies. Specifically, these
 495 anomalies are of $\ln(Y)$ in scenarios where the activation rate is not considered and of $\ln(N_d)$
 496 in scenarios where the activation rate is included. The term $\hat{\sigma}^2$ denotes the mean of squared
 497 residuals of the regression model and we estimate $N_{\text{nom}}/N_{\text{eff}}$ as $(1 + r)/(1 - r)$, where r is
 498 the lag one autocorrelation of CRE_lcl'd'.

499

500 Uncertainty for spatially averaged regression coefficients is calculated as

$$501 \quad \Delta_{\text{obs}} = \sqrt{\frac{\sum_{k=1}^{N_{\text{nom}}^*} (\delta_k w_k)^2}{\left(\sum_{k=1}^{N_{\text{nom}}^*} w_k\right)^2}} \sqrt{\frac{N_{\text{nom}}^*}{N_{\text{eff}}^*}}, \quad (\text{A10})$$

502 where δ_k denotes the uncertainty of the k^{th} grid box, w_k is the cosine of the latitude. N_{nom}^*
 503 represents the nominal number of spatial degrees of freedom, while N_{eff}^* represents the
 504 effective number of spatial degrees of freedom. The ratio $N_{\text{nom}}^*/N_{\text{eff}}^*$ is determined through
 505 empirical orthogonal function (EOF) analysis applied to CRE_lcl'd' for all ocean grid boxes
 506 between 50°S and 50°N as outlined in equation 5 of Bretherton et al. (1999). Before conducting
 507 the EOF analysis, each grid of CRE_lcl'd' value is multiplied by $\sqrt{w_k}$ to mitigate dependencies
 508 on grid geometry (North et al. 1982). The derived value of Δ_{obs} quantifies the half-width of the
 509 90% CI for ERFaci_obs over our domain region specifically reflecting the uncertainty
 510 associated with regression coefficients.

511



512 To estimate uncertainty derived from model predictions, we examine the entire range of aerosol
513 concentration changes across each CMIP6 model, instead of estimating uncertainty within the
514 5th-95th percentile range, primarily due to the limited number of models available for our
515 analysis: 13 models for $\Delta \ln(\text{SO}_4)$ and 9 models for $\Delta \ln(\text{Al})$. This decision reflects a
516 methodological adaptation to the limited model dataset, ensuring a comprehensive evaluation
517 of model-derived uncertainty (Myers et al., 2021). We first calculate ERFaci_obs by
518 multiplying $\Delta \ln(Y)$ from each of the models by the observationally derived susceptibility. The
519 half-width of the CI, denoted as Δ_{model} , is derived by halving the difference between the
520 maximum and minimum estimates of ERFaci_obs . The overall 90% CI is determined by

521
$$\text{ERFaci_obs, domain} \pm \sqrt{\Delta_{\text{obs}}^2 + \Delta_{\text{model}}^2}.$$

522

523 In our methodology, the scalar γ is used to extrapolate the global ERFaci_obs from our domain-
524 specific ERFaci_obs estimates. This extrapolation introduces an additional component of
525 uncertainty. Although both γ and the changes in aerosol concentration are obtained from
526 CMIP6 model outputs, it's important to note that γ does not directly correlate with aerosol
527 concentration changes across the models. Consequently, the uncertainty associated with γ is
528 quantified using the root mean squared error (RMSE) between the domain-specific averaged
529 ERFaci_true , multiplied by γ , and the global-mean ERFaci_true . The overall 90% CI is
530 determined by $\text{ERFaci_obs, global} \pm \sqrt{([\gamma]\Delta_{\text{obs}})^2 + ([\gamma]\Delta_{\text{model}})^2 + \Delta_{\gamma}^2}$, where square
531 brackets indicate multi-model mean of a parameter.

532

533

534 **Author Contributions:** B.J.S. designed research; C.P. performed research; C.P. analyzed
535 data; B.J.S., R.J.K., T.S.L., and H.H. contributed ideas; C.P., B.J.S., R.J.K., T.S.L., and H.H.
536 wrote the paper.

537

538 **Competing Interest Statement:** The authors declare no competing interest.

539

540 Acknowledgements

541 We greatly wish to thank Casey J. Wall for sharing the post-processed CERES and MERRA-
542 2 reanalysis data used in Wall et al. (2022), and Edward Gryspeerd for sharing data related to



543 cloud droplet number concentration. C.P. and B.J.S. were supported by the National Oceanic
544 and Atmospheric Administration Climate Program Office's Modeling, Analysis, Predictions,
545 and Projections Program Grant NA21OAR4310351. R.J.K. was supported by NASA Science
546 of Terra, Aqua and Suomi-NPP grant no. 80NSSC21K1968. T.S.L. was supported by National
547 Aeronautics and Space Administration CloudSat Grant G-39690-1.

548

549 **Data Availability**

550 CERES data were downloaded from the National Aeronautics and Space Administration
551 (NASA) CERES ordering tool (<https://ceres.larc.nasa.gov/data/>). MODIS data were
552 downloaded from NASA Level-1 and Atmosphere Archive and Distribution System
553 (<https://ladsweb.modaps.eosdis.nasa.gov/archive/allData>). MODIS N_d data are available from
554 the Centre for Environmental Data Analysis
555 (<https://doi.org/10.5285/864a46cc65054008857ee5bb772a2a2b>, Gryspeerdt et al., 2022).
556 MERRA-2 reanalysis data were downloaded from NASA Goddard Earth Sciences Data and
557 Information Services Center (<https://doi.org/10.5067/LTVB4GPCOTK2>). The CMIP6 data
558 used in this study are available at the Earth System Grid Federation data portal ([https://esgf-
560 node.llnl.gov/projects/cmip6/](https://esgf-
559 node.llnl.gov/projects/cmip6/)). Intermediate data products used in our analysis, including
560 gridded monthly anomalies and regression coefficients, are available from GitHub
561 (https://github.com/nicklutsko/Radiative_Forcing_Aerosol_Clouds, Wall et al., 2022).

562

563 **References**

564 Aas, W., Mortier, A., Bowersox, V., Cherian, R., Faluvegi, G., Fagerli, H., Hand, J., Klimont,
565 Z., Galy-Lacaux, C., Lehmann, C. M. B., Myhre, C. L., Myhre, G., Olivié, D., Sato, K.,
566 Quaas, J., Rao, P. S. P., Schulz, M., Shindell, D., Skeie, R. B., Stein, A., Takemura, T., Tsyro,
567 S., Vet, R., and Xu, X.: Global and regional trends of atmospheric sulfur, *Sci Rep*, 9, 953,
568 <https://doi.org/10.1038/s41598-018-37304-0>, 2019.

569 Albrecht, B. A.: Aerosols, Cloud Microphysics, and Fractional Cloudiness, *Science*, 245,
570 1227–1230, <https://doi.org/10.1126/science.245.4923.1227>, 1989.

571 Boucher, O., Randall, D., Artaxo, P., Bretherton, C., Feingold, G., Forster, P., Kerminen, V.-
572 M., Kondo, Y., Liao, H., Lohmann, U., Rasch, P., Satheesh, S.K., Sherwood, S., Stevens, B.,
573 and Zhang, X.Y.: Clouds and aerosols, in: *Climate Change 2013: The Physical Science Basis*.



- 574 Contribution of Working Group I to the Fifth Assessment Report of the Intergovernmental
575 Panel on Climate Change, edited by: Stocker, T.F., Qin, D., Plattner, G.-K., Tignor, M., Allen,
576 S.K., Doschung, J., Nauels, A., Xia, Y., Bex, V., and Midgley, P.M., Cambridge University
577 Press, Cambridge, UK and New York, NY, USA, 571-657,
578 <https://doi.org/10.1017/CBO9781107415324.016>, 2013.
- 579 Bellouin, N., Quaas, J., Gryspeerdt, E., Kinne, S., Stier, P., Watson-Parris, D., Boucher, O.,
580 Carslaw, K. S., Christensen, M., Daniau, A.-L., Dufresne, J.-L., Feingold, G., Fiedler, S.,
581 Forster, P., Gettelman, A., Haywood, J. M., Lohmann, U., Malavelle, F., Mauritsen, T.,
582 McCoy, D. T., Myhre, G., Mülmenstädt, J., Neubauer, D., Possner, A., Rugenstein, M., Sato,
583 Y., Schulz, M., Schwartz, S. E., Sourdeval, O., Storelvmo, T., Toll, V., Winker, D., and
584 Stevens, B.: Bounding Global Aerosol Radiative Forcing of Climate Change, *Reviews of*
585 *Geophysics*, 58, e2019RG000660, <https://doi.org/10.1029/2019RG000660>, 2020.
- 586 Bennartz, R. and Rausch, J.: Global and regional estimates of warm cloud droplet number
587 concentration based on 13 years of AQUA-MODIS observations, *Atmospheric Chemistry and*
588 *Physics*, 17, 9815–9836, <https://doi.org/10.5194/acp-17-9815-2017>, 2017.
- 589 Boucher, O. and Lohmann, U.: The sulfate-CCN-cloud albedo effect: A sensitivity study with
590 two general circulation models, 47, 281, <https://doi.org/10.3402/tellusb.v47i3.16048>, 1995.
- 591 Bretherton, C. S., Widmann, M., Dymnikov, V. P., Wallace, J. M., and Bladé, I.: The Effective
592 Number of Spatial Degrees of Freedom of a Time-Varying Field, *Journal of Climate*, 12,
593 1990–2009, [https://doi.org/10.1175/1520-0442\(1999\)012<1990:TENOSD>2.0.CO;2](https://doi.org/10.1175/1520-0442(1999)012<1990:TENOSD>2.0.CO;2), 1999.
- 594 Brunner, L., Pendergrass, A. G., Lehner, F., Merrifield, A. L., Lorenz, R., and Knutti, R.:
595 Reduced global warming from CMIP6 projections when weighting models by performance
596 and independence, *Earth System Dynamics*, 11, 995–1012, [https://doi.org/10.5194/esd-11-](https://doi.org/10.5194/esd-11-995-2020)
597 995-2020, 2020.
- 598 Ceppi, P. and Nowack, P.: Observational evidence that cloud feedback amplifies global
599 warming, *Proceedings of the National Academy of Sciences*, 118, e2026290118,
600 <https://doi.org/10.1073/pnas.2026290118>, 2021.
- 601 Charlson, R. J., Schwartz, S. E., Hales, J. M., Cess, R. D., Coakley, J. A., Hansen, J. E., and
602 Hofmann, D. J.: Climate Forcing by Anthropogenic Aerosols, *Science*, 255, 423–430,
603 <https://doi.org/10.1126/science.255.5043.423>, 1992.



- 604 Christensen, M. W., Chen, Y.-C., and Stephens, G. L.: Aerosol indirect effect dictated by
605 liquid clouds, *Journal of Geophysical Research: Atmospheres*, 121, 14,636–14,650,
606 <https://doi.org/10.1002/2016JD025245>, 2016.
- 607 Chung, E.-S. and Soden, B. J.: Hemispheric climate shifts driven by anthropogenic aerosol–
608 cloud interactions, *Nature Geosci*, 10, 566–571, <https://doi.org/10.1038/ngeo2988>, 2017.
- 609 Dentener, F.J., Hall, B., and Smith, C.: Annex III: Tables of Historical and Projected Well-
610 mixed Greenhouse Gas Mixing Ratios and Effective Radiative Forcing of All Climate
611 Forcers, in: *Climate Change 2021 – The Physical Science Basis: Working Group I*
612 *Contribution to the Sixth Assessment Report of the Intergovernmental Panel on Climate*
613 *Change*, Cambridge University Press, 2139–2152, 2023.
- 614 Douglas, A. and L’Ecuyer, T.: Quantifying variations in shortwave aerosol–cloud–radiation
615 interactions using local meteorology and cloud state constraints, *Atmospheric Chemistry and*
616 *Physics*, 19, 6251–6268, <https://doi.org/10.5194/acp-19-6251-2019>, 2019.
- 617 Douglas, A. and L’Ecuyer, T.: Quantifying cloud adjustments and the radiative forcing due to
618 aerosol–cloud interactions in satellite observations of warm marine clouds, *Atmospheric*
619 *Chemistry and Physics*, 20, 6225–6241, <https://doi.org/10.5194/acp-20-6225-2020>, 2020.
- 620 Forster, P., Ramaswamy, V., Artaxo, P., Berntsen, T., Betts, R., Fahey, D.W., Haywood, J.,
621 Lean, J., Lowe, D.C., Myhre, G., Nganga, J., Prinn, R., Raga, G., Schulz, M., and Van
622 Dorland, R.: Changes in Atmospheric Constituents and in Radiative Forcing, in: *Climate*
623 *Change 2007: The Physical Science Basis. Contribution of Working Group I to the Fourth*
624 *Assessment Report of the Intergovernmental Panel on Climate Change*, edited by: Solomon,
625 S., Qin, D., Manning, M., Chen, Z., Marquis, M., Averyt, K.B., Tignor, M., and Miller, H.L.,
626 Cambridge University Press, Cambridge, UK and New York, NY, USA, 2007.
- 627 Forster, P., Storelvmo, T., Armour, K., Collins, W., Dufresne, J.-L., Frame, D., Lunt, D.J.,
628 Mauritsen, T., Palmer, M.D., Watanabe, M., Wild, M., and Zhang, H.: The Earth’s Energy
629 Budget, Climate Feedbacks, and Climate Sensitivity, in: *Climate Change 2021: The Physical*
630 *Science Basis. Contribution of Working Group I to the Sixth Assessment Report of the*
631 *Intergovernmental Panel on Climate Change*, edited by: Masson-Delmotte, V., Zhai, P.,
632 Pirani, A., Connors, S.L., Péan, C., Berger, S., Caud, N., Chen, Y., Goldfarb, L., Gomis, M.I.,
633 Huang, M., Leitzell, K., Lonnoy, E., Matthews, J.B.R., Maycock, T.K., Waterfield, T.,



- 634 Yelekçi, O., Yu, R., and Zhou, B., Cambridge University Press, Cambridge, UK and New
635 York, NY, USA, 923–1054, <https://doi.org/10.1017/9781009157896.009>, 2021.
- 636 Gelaro, R., McCarty, W., Suárez, M. J., Todling, R., Molod, A., Takacs, L., Randles, C. A.,
637 Darmenov, A., Bosilovich, M. G., Reichle, R., Wargan, K., Coy, L., Cullather, R., Draper, C.,
638 Akella, S., Buchard, V., Conaty, A., Silva, A. M. da, Gu, W., Kim, G.-K., Koster, R.,
639 Lucchesi, R., Merkova, D., Nielsen, J. E., Partyka, G., Pawson, S., Putman, W., Rienecker,
640 M., Schubert, S. D., Sienkiewicz, M., and Zhao, B.: The Modern-Era Retrospective Analysis
641 for Research and Applications, Version 2 (MERRA-2), *Journal of Climate*, 30, 5419–5454,
642 <https://doi.org/10.1175/JCLI-D-16-0758.1>, 2017.
- 643 Gryspeerdt, E., Quaas, J., and Bellouin, N.: Constraining the aerosol influence on cloud
644 fraction, *Journal of Geophysical Research: Atmospheres*, 121, 3566–3583,
645 <https://doi.org/10.1002/2015JD023744>, 2016.
- 646 Gryspeerdt, E., Quaas, J., Ferrachat, S., Gettelman, A., Ghan, S., Lohmann, U., Morrison, H.,
647 Neubauer, D., Partridge, D. G., Stier, P., Takemura, T., Wang, H., Wang, M., and Zhang, K.:
648 Constraining the instantaneous aerosol influence on cloud albedo, *Proceedings of the*
649 *National Academy of Sciences*, 114, 4899–4904, <https://doi.org/10.1073/pnas.1617765114>,
650 2017.
- 651 Gryspeerdt, E., Goren, T., Sourdeval, O., Quaas, J., Mülmenstädt, J., Dipu, S., Unglaub, C.,
652 Gettelman, A., and Christensen, M.: Constraining the aerosol influence on cloud liquid water
653 path, *Atmospheric Chemistry and Physics*, 19, 5331–5347, [https://doi.org/10.5194/acp-19-](https://doi.org/10.5194/acp-19-5331-2019)
654 [5331-2019](https://doi.org/10.5194/acp-19-5331-2019), 2019.
- 655 Gryspeerdt, E., McCoy, D. T., Crosbie, E., Moore, R. H., Nott, G. J., Painemal, D., Small-
656 Griswold, J., Sorooshian, A., and Ziemba, L.: The impact of sampling strategy on the cloud
657 droplet number concentration estimated from satellite data, *Atmospheric Measurement*
658 *Techniques*, 15, 3875–3892, <https://doi.org/10.5194/amt-15-3875-2022>, 2022.
- 659 Hasekamp, O. P., Gryspeerdt, E., and Quaas, J.: Analysis of polarimetric satellite
660 measurements suggests stronger cooling due to aerosol-cloud interactions, *Nat Commun*, 10,
661 5405, <https://doi.org/10.1038/s41467-019-13372-2>, 2019.
- 662 Hoesly, R. M., Smith, S. J., Feng, L., Klimont, Z., Janssens-Maenhout, G., Pitkanen, T.,
663 Seibert, J. J., Vu, L., Andres, R. J., Bolt, R. M., Bond, T. C., Dawidowski, L., Kholod, N.,



- 664 Kurokawa, J., Li, M., Liu, L., Lu, Z., Moura, M. C. P., O'Rourke, P. R., and Zhang, Q.:
665 Historical (1750–2014) anthropogenic emissions of reactive gases and aerosols from the
666 Community Emissions Data System (CEDS), *Geoscientific Model Development*, 11, 369–
667 408, <https://doi.org/10.5194/gmd-11-369-2018>, 2018.
- 668 Jia, H. and Quaas, J.: Nonlinearity of the cloud response postpones climate penalty of
669 mitigating air pollution in polluted regions, *Nat. Clim. Chang.*, 13, 943–950,
670 <https://doi.org/10.1038/s41558-023-01775-5>, 2023.
- 671 Jia, H., Ma, X., Quaas, J., Yin, Y., and Qiu, T.: Is positive correlation between cloud droplet
672 effective radius and aerosol optical depth over land due to retrieval artifacts or real physical
673 processes?, *Atmospheric Chemistry and Physics*, 19, 8879–8896, [https://doi.org/10.5194/acp-](https://doi.org/10.5194/acp-19-8879-2019)
674 [19-8879-2019](https://doi.org/10.5194/acp-19-8879-2019), 2019.
- 675 Knutti, R., Sedláček, J., Sanderson, B. M., Lorenz, R., Fischer, E. M., and Eyring, V.: A
676 climate model projection weighting scheme accounting for performance and interdependence,
677 *Geophysical Research Letters*, 44, 1909–1918, <https://doi.org/10.1002/2016GL072012>, 2017.
- 678 Kramer, R. J., He, H., Soden, B. J., Oreopoulos, L., Myhre, G., Forster, P. M., and Smith, C.
679 J.: Observational Evidence of Increasing Global Radiative Forcing, *Geophysical Research*
680 *Letters*, 48, e2020GL091585, <https://doi.org/10.1029/2020GL091585>, 2021.
- 681 Lenssen, N. J. L., Schmidt, G. A., Hansen, J. E., Menne, M. J., Persin, A., Ruedy, R., and
682 Zyss, D.: Improvements in the GISTEMP Uncertainty Model, *Journal of Geophysical*
683 *Research: Atmospheres*, 124, 6307–6326, <https://doi.org/10.1029/2018JD029522>, 2019.
- 684 McCoy, D. T., Bender, F. A.-M., Grosvenor, D. P., Mohrmann, J. K., Hartmann, D. L., Wood,
685 R., and Field, P. R.: Predicting decadal trends in cloud droplet number concentration using
686 reanalysis and satellite data, *Atmospheric Chemistry and Physics*, 18, 2035–2047,
687 <https://doi.org/10.5194/acp-18-2035-2018>, 2018.
- 688 Mülmenstädt, J. and Feingold, G.: The Radiative Forcing of Aerosol–Cloud Interactions in
689 Liquid Clouds: Wrestling and Embracing Uncertainty, *Curr Clim Change Rep*, 4, 23–40,
690 <https://doi.org/10.1007/s40641-018-0089-y>, 2018.
- 691 Myers, T. A., Scott, R. C., Zelinka, M. D., Klein, S. A., Norris, J. R., and Caldwell, P. M.:
692 Observational constraints on low cloud feedback reduce uncertainty of climate sensitivity,
693 *Nat. Clim. Chang.*, 11, 501–507, <https://doi.org/10.1038/s41558-021-01039-0>, 2021.



- 694 North, G. R., Bell, T. L., Cahalan, R. F., and Moeng, F. J.: Sampling Errors in the Estimation
695 of Empirical Orthogonal Functions, *Monthly Weather Review*, 110, 699–706,
696 [https://doi.org/10.1175/1520-0493\(1982\)110<0699:SEITEO>2.0.CO;2](https://doi.org/10.1175/1520-0493(1982)110<0699:SEITEO>2.0.CO;2), 1982.
- 697 Painemal, D., Chiu, J.-Y. C., Minnis, P., Yost, C., Zhou, X., Cadeddu, M., Eloranta, E., Lewis,
698 E. R., Ferrare, R., and Kollias, P.: Aerosol and cloud microphysics covariability in the
699 northeast Pacific boundary layer estimated with ship-based and satellite remote sensing
700 observations, *Journal of Geophysical Research: Atmospheres*, 122, 2403–2418,
701 <https://doi.org/10.1002/2016JD025771>, 2017.
- 702 Pincus, R. and Baker, M. B.: Effect of precipitation on the albedo susceptibility of clouds in
703 the marine boundary layer, *Nature*, 372, 250–252, <https://doi.org/10.1038/372250a0>, 1994.
- 704 Pincus, R., Forster, P. M., and Stevens, B.: The Radiative Forcing Model Intercomparison
705 Project (RFMIP): experimental protocol for CMIP6, *Geoscientific Model Development*, 9,
706 3447–3460, <https://doi.org/10.5194/gmd-9-3447-2016>, 2016.
- 707 Pincus, R., Hubanks, P. A., Platnick, S., Meyer, K., Holz, R. E., Botambekov, D., and Wall, C.
708 J.: Updated observations of clouds by MODIS for global model assessment, *Earth System
709 Science Data*, 15, 2483–2497, <https://doi.org/10.5194/essd-15-2483-2023>, 2023.
- 710 Raghuraman, S. P., Paynter, D., and Ramaswamy, V.: Anthropogenic forcing and response
711 yield observed positive trend in Earth’s energy imbalance, *Nat Commun*, 12, 4577,
712 <https://doi.org/10.1038/s41467-021-24544-4>, 2021.
- 713 Randles, C. A., Silva, A. M. da, Buchard, V., Colarco, P. R., Darmenov, A., Govindaraju, R.,
714 Smirnov, A., Holben, B., Ferrare, R., Hair, J., Shinozuka, Y., and Flynn, C. J.: The MERRA-2
715 Aerosol Reanalysis, 1980 Onward. Part I: System Description and Data Assimilation
716 Evaluation, *Journal of Climate*, 30, 6823–6850, <https://doi.org/10.1175/JCLI-D-16-0609.1>,
717 2017.
- 718 Rosenfeld, D.: Aerosols, Clouds, and Climate, *Science*, 312, 1323–1324,
719 <https://doi.org/10.1126/science.1128972>, 2006.
- 720 Saponaro, G., Sporre, M. K., Neubauer, D., Kokkola, H., Kolmonen, P., Sogacheva, L., Arola,
721 A., de Leeuw, G., Karset, I. H. H., Laaksonen, A., and Lohmann, U.: Evaluation of aerosol
722 and cloud properties in three climate models using MODIS observations and its
723 corresponding COSP simulator, as well as their application in aerosol–cloud interactions,



724 Atmospheric Chemistry and Physics, 20, 1607–1626, <https://doi.org/10.5194/acp-20-1607->
725 2020, 2020.

726 Scott, R. C., Myers, T. A., Norris, J. R., Zelinka, M. D., Klein, S. A., Sun, M., and Doelling,
727 D. R.: Observed Sensitivity of Low-Cloud Radiative Effects to Meteorological Perturbations
728 over the Global Oceans, *Journal of Climate*, 33, 7717–7734, <https://doi.org/10.1175/JCLI-D->
729 19-1028.1, 2020.

730 Sherwood, S. C., Webb, M. J., Annan, J. D., Armour, K. C., Forster, P. M., Hargreaves, J. C.,
731 Hegerl, G., Klein, S. A., Marvel, K. D., Rohling, E. J., Watanabe, M., Andrews, T.,
732 Braconnot, P., Bretherton, C. S., Foster, G. L., Hausfather, Z., von der Heydt, A. S., Knutti,
733 R., Mauritsen, T., Norris, J. R., Proistosescu, C., Rugenstein, M., Schmidt, G. A., Tokarska,
734 K. B., and Zelinka, M. D.: An Assessment of Earth’s Climate Sensitivity Using Multiple
735 Lines of Evidence, *Reviews of Geophysics*, 58, e2019RG000678,
736 <https://doi.org/10.1029/2019RG000678>, 2020.

737 Smith, C. J., Kramer, R. J., Myhre, G., Alterskjær, K., Collins, W., Sima, A., Boucher, O.,
738 Dufresne, J.-L., Nabat, P., Michou, M., Yukimoto, S., Cole, J., Paynter, D., Shiogama, H.,
739 O’Connor, F. M., Robertson, E., Wiltshire, A., Andrews, T., Hannay, C., Miller, R.,
740 Nazarenko, L., Kirkevåg, A., Olivie, D., Fiedler, S., Lewinschal, A., Mackallah, C., Dix, M.,
741 Pincus, R., and Forster, P. M.: Effective radiative forcing and adjustments in CMIP6 models,
742 *Atmospheric Chemistry and Physics*, 20, 9591–9618, <https://doi.org/10.5194/acp-20-9591->
743 2020, 2020a.

744 Smith, C. J., Kramer, R. J., and Sima, A.: The HadGEM3-GA7.1 radiative kernel: the
745 importance of a well-resolved stratosphere, *Earth System Science Data*, 12, 2157–2168,
746 <https://doi.org/10.5194/essd-12-2157-2020>, 2020b.

747 Soden, B. and Chung, E.-S.: The Large-Scale Dynamical Response of Clouds to Aerosol
748 Forcing, *Journal of Climate*, 30, 8783–8794, <https://doi.org/10.1175/JCLI-D-17-0050.1>,
749 2017.

750 Soden, B. J. and Vecchi, G. A.: The vertical distribution of cloud feedback in coupled ocean-
751 atmosphere models, *Geophysical Research Letters*, 38,
752 <https://doi.org/10.1029/2011GL047632>, 2011.



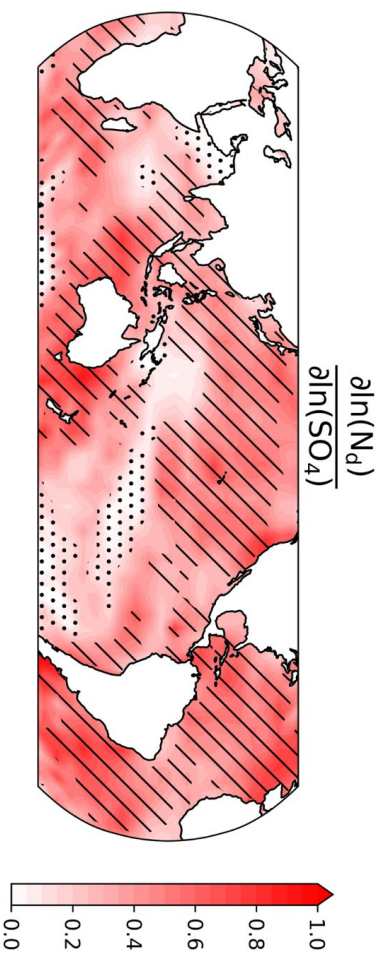
- 753 Soden, B. J., Held, I. M., Colman, R., Shell, K. M., Kiehl, J. T., and Shields, C. A.:
754 Quantifying Climate Feedbacks Using Radiative Kernels, *Journal of Climate*, 21, 3504–3520,
755 <https://doi.org/10.1175/2007JCLI2110.1>, 2008.
- 756 Stier, P.: Limitations of passive remote sensing to constrain global cloud condensation nuclei,
757 *Atmospheric Chemistry and Physics*, 16, 6595–6607, [https://doi.org/10.5194/acp-16-6595-](https://doi.org/10.5194/acp-16-6595-2016)
758 2016, 2016.
- 759 Storch, H. von and Zwiers, F. W.: *Statistical Analysis in Climate Research*, Cambridge
760 University Press, Cambridge, <https://doi.org/10.1017/CBO9780511612336>, 1999.
- 761 Twomey, S.: The Influence of Pollution on the Shortwave Albedo of Clouds, *Journal of the*
762 *Atmospheric Sciences*, 34, 1149–1152, [https://doi.org/10.1175/1520-](https://doi.org/10.1175/1520-0469(1977)034<1149:TIOPOT>2.0.CO;2)
763 0469(1977)034<1149:TIOPOT>2.0.CO;2, 1977.
- 764 Wall, C. J., Norris, J. R., Possner, A., McCoy, D. T., McCoy, I. L., and Lutsko, N. J.:
765 Assessing effective radiative forcing from aerosol–cloud interactions over the global ocean,
766 *Proceedings of the National Academy of Sciences*, 119, e2210481119,
767 <https://doi.org/10.1073/pnas.2210481119>, 2022.
- 768 Wall, C. J., Storelvmo, T., and Possner, A.: Global observations of aerosol indirect effects
769 from marine liquid clouds, *Atmospheric Chemistry and Physics*, 23, 13125–13141,
770 <https://doi.org/10.5194/acp-23-13125-2023>, 2023.
- 771 Wang, C., Soden, B. J., Yang, W., and Vecchi, G. A.: Compensation Between Cloud Feedback
772 and Aerosol-Cloud Interaction in CMIP6 Models, *Geophysical Research Letters*, 48,
773 e2020GL091024, <https://doi.org/10.1029/2020GL091024>, 2021.
- 774 Webb, M. J., Senior, C. A., Sexton, D. M. H., Ingram, W. J., Williams, K. D., Ringer, M. A.,
775 McAvaney, B. J., Colman, R., Soden, B. J., Gudgel, R., Knutson, T., Emori, S., Ogura, T.,
776 Tsushima, Y., Andronova, N., Li, B., Musat, I., Bony, S., and Taylor, K. E.: On the
777 contribution of local feedback mechanisms to the range of climate sensitivity in two GCM
778 ensembles, *Clim Dyn*, 27, 17–38, <https://doi.org/10.1007/s00382-006-0111-2>, 2006.
- 779 Wenzel, S., Eyring, V., Gerber, E. P., and Karpechko, A. Y.: Constraining Future Summer
780 Austral Jet Stream Positions in the CMIP5 Ensemble by Process-Oriented Multiple
781 Diagnostic Regression, <https://doi.org/10.1175/JCLI-D-15-0412.1>, 2016.



- 782 Wood, R., Leon, D., Lebsock, M., Snider, J., and Clarke, A. D.: Precipitation driving of
783 droplet concentration variability in marine low clouds, *Journal of Geophysical Research:*
784 *Atmospheres*, 117, <https://doi.org/10.1029/2012JD018305>, 2012.
- 785 Zelinka, M. D., Andrews, T., Forster, P. M., and Taylor, K. E.: Quantifying components of
786 aerosol-cloud-radiation interactions in climate models, *Journal of Geophysical Research:*
787 *Atmospheres*, 119, 7599–7615, <https://doi.org/10.1002/2014JD021710>, 2014.
- 788 Zhang, Z. and Platnick, S.: An assessment of differences between cloud effective particle
789 radius retrievals for marine water clouds from three MODIS spectral bands, *Journal of*
790 *Geophysical Research: Atmospheres*, 116, <https://doi.org/10.1029/2011JD016216>, 2011.



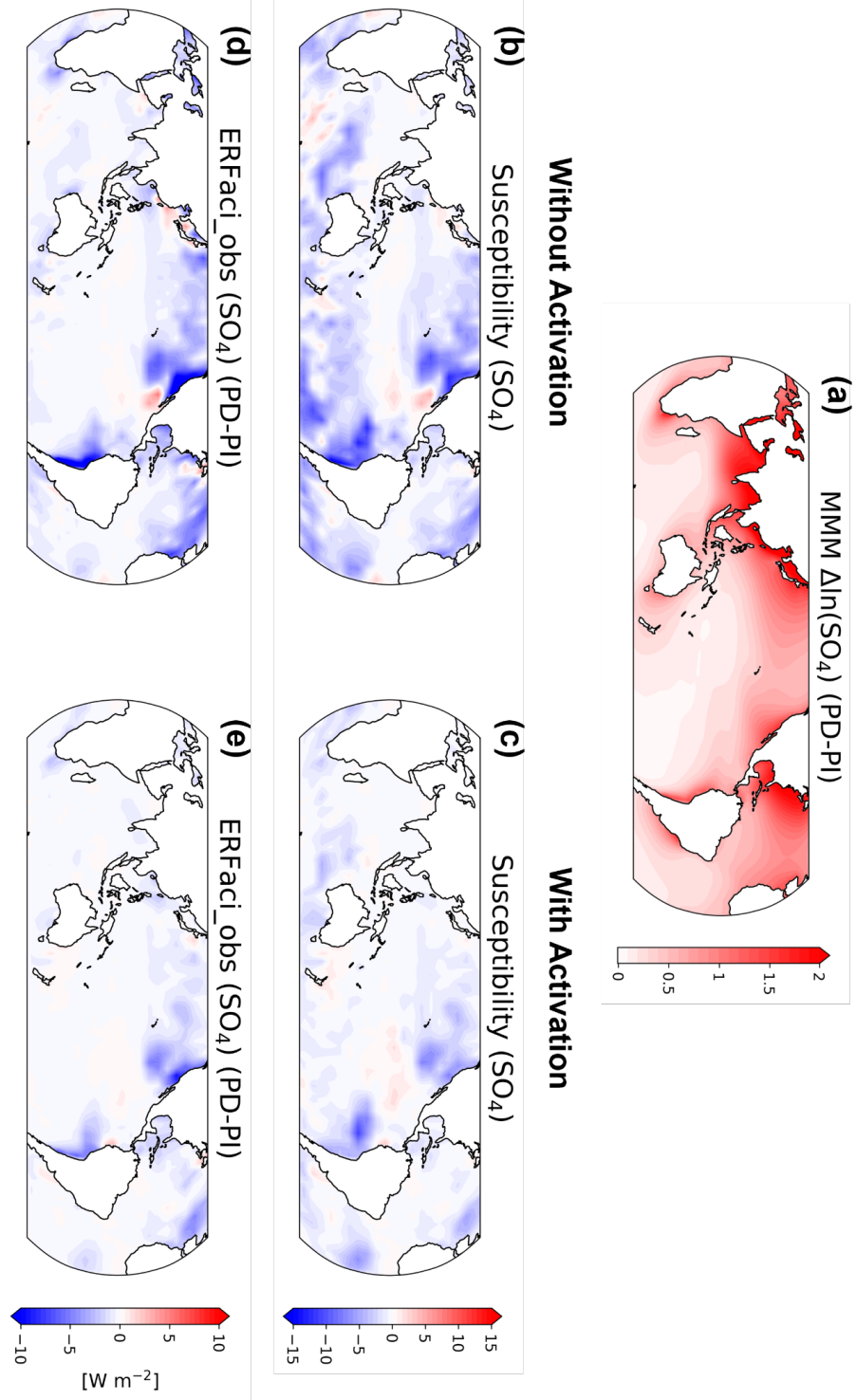
791 **Figures**



792

793 **Fig. 1.** Regression coefficient map of the activation rate of cloud droplet number concentration (N_d) to sulfate aerosol
 794 concentration (SO_4). The color scale indicates the magnitude of sensitivity, where an increase in SO_4 concentration
 795 corresponds to an increase in N_d . Areas with diagonal indicate correlation coefficients exceeding 0.4, demonstrating a
 796 significantly high linearity between SO_4 and N_d . Areas with stippling indicate where the changes are not statistically
 797 different from zero at the 95% confidence level using a Student's t-test.

798



799

800 **Fig. 2.** Spatial distribution of ERFaci_obs components and the estimated ERFaci_obs differentiated by the consideration of



801 the activation rate. (a) Multi-model mean (MMM) of changes in SO₄ concentration between pre-industrial (PI) and present-
802 day (PD) periods. 13 models are used for this analysis (Table A1). (b,c) Susceptibility of low cloud radiative effect to SO₄
803 concentration derived from CCF analysis using observations (Appendix A). (d,e) Observationally constrained ERF_{aci} for
804 SO₄ estimated by multiplying the susceptibility with the changes in SO₄ concentration.

805

806

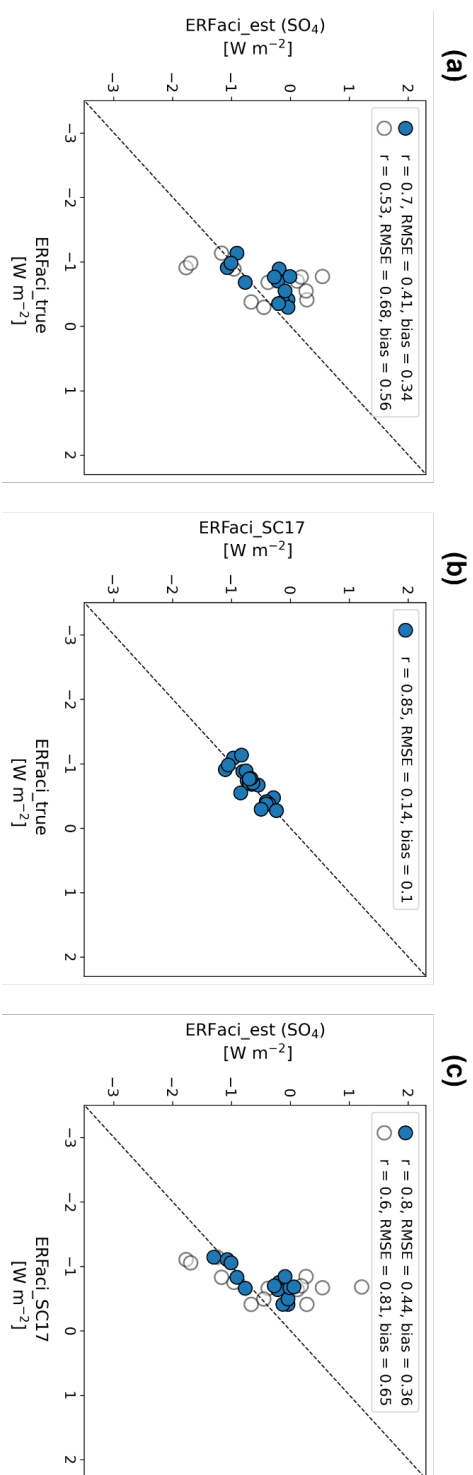
807

808

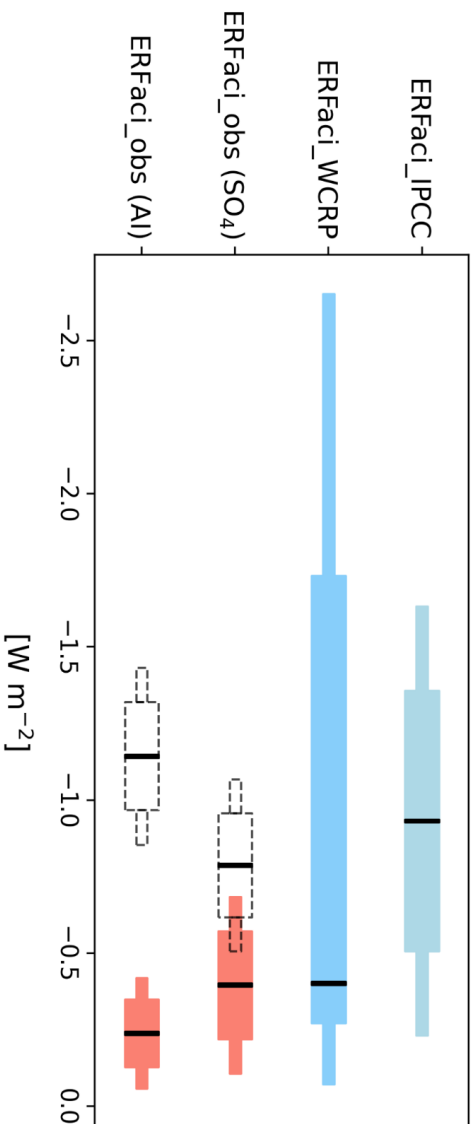
809

810

811



812 **Fig. 3.** “Perfect-model” cross validation analysis of global-mean ERFaci estimates. (a) ERFaci_{true} versus ERFaci_{est}
 813 which is estimated by simplified version of equations (1) and (2) (Appendix A), (b) ERFaci_{true} versus ERFaci estimates
 814 obtained using the method proposed by Soden and Chung (2017; SC17), and (c) ERFaci_{SC17} versus ERFaci_{est}. Filled
 815 blue circles represent estimates where the activation rate is considered, and open grey circles represent estimates without
 816 activation rate consideration. The correlation coefficient (r), Root Mean Square Error (RMSE), and bias are displayed in
 817 the upper left corner of each panel. Bias is defined as the mean absolute difference from the 1:1 reference line, depicted by
 818 a dashed line. All panels have identical x and y axis ranges to highlight the variance among the estimation methods. Higher
 819 r values, lower RMSE, and minimal bias indicate consistency in ERFaci estimates across different estimation methods using
 820 CMIP6 models.
 821



822

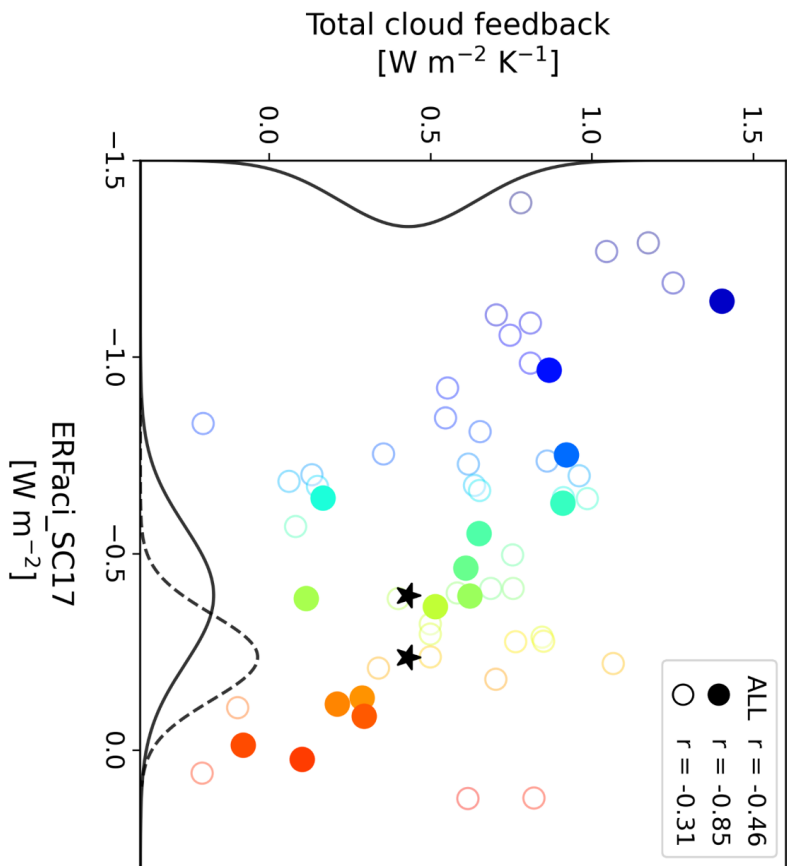
823 **Fig. 4.** Estimates of globally averaged ERFaci values, including those from the IPCC Sixth Assessment Report, from WCRP
 824 assessment, ERFaci_obs for SO₄, and ERFaci_obs for AI. The ERFaci_obs estimates considering activation rate are shown
 825 in red, while those not considering activation rate are displayed in dashed grey. Thin and thick bars represent the 90% and
 826 66% confidence intervals (CI), respectively, except for the WCRP estimate of ERFaci, which shows 68% CI for the thick
 827 bar. The black vertical lines indicate the best estimate of each ERFaci. The ERFaci values from the IPCC represent the
 828 assessment based on observational evidence alone.

829

830



831



832

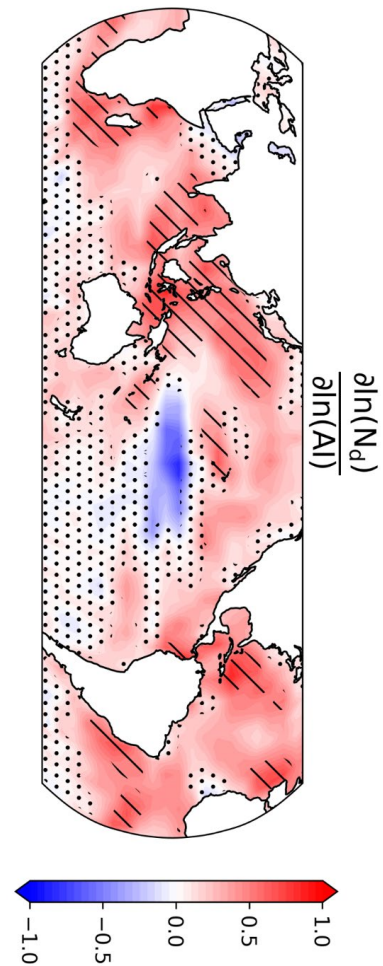
833 **Fig. 5.** Correlation between global-mean ERFaci estimates obtained using the method proposed by Soden and Chung (2017);

834 SC17), aimed at expanding the model availability, and the globally averaged total cloud feedback as determined by the
835 corresponding models. Each dot represents a single model. The colors from red to blue indicate weak ERFaci models to
836 strong negative ERFaci models. Filled circles represent the 15 'GOOD HIST' models that align more closely with historical
837 observations of global-mean surface warming, whereas open circles denote the remaining models (Appendix A).
838 Correlation coefficients (r) for the entire models, the 'GOOD HIST' models, and remaining models are shown in the upper
839 right corner. The probability density functions (PDFs) showing the 90% confidence intervals for observationally constrained
840 ERFaci from sulfate concentration (SO_4 ; solid line) and the aerosol index (AI; dashed line) are plotted along the x-axis,
841 while the PDF for observationally constrained total cloud feedback (solid line), derived from Ceppi and Nowack (2021), is
842 plotted on the y-axis (amplitudes scaled arbitrarily). Stars denote the best estimates of the PDFs, signifying the most
843 probable values within the distributions.

844

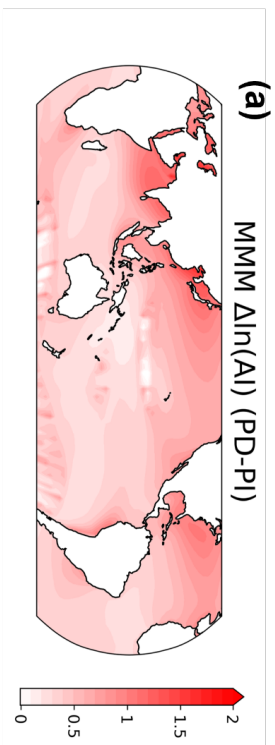
845





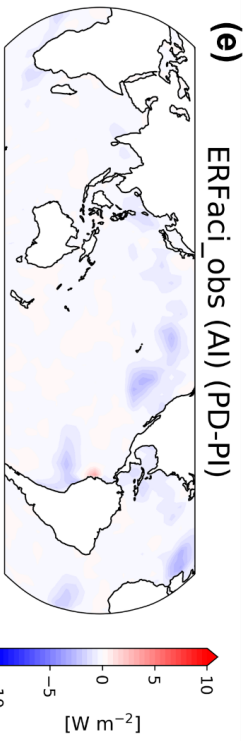
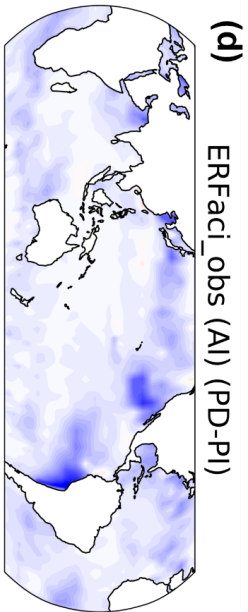
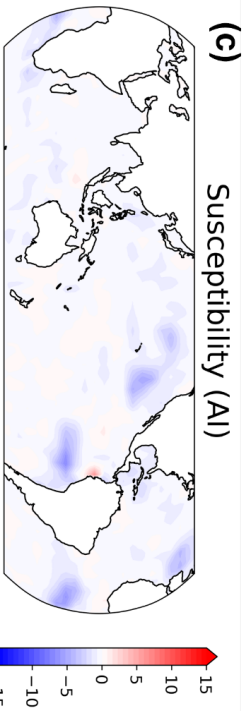
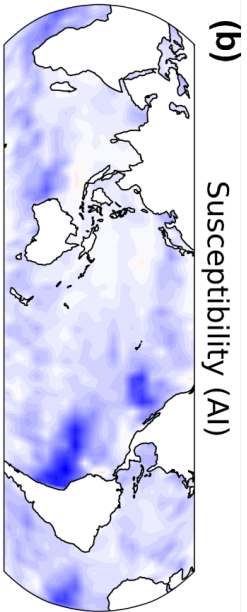
846
847 **Fig. A1.** Same as Fig. 1 but for AI.

848
849
850
851
852
853



Without Activation

With Activation



854

35



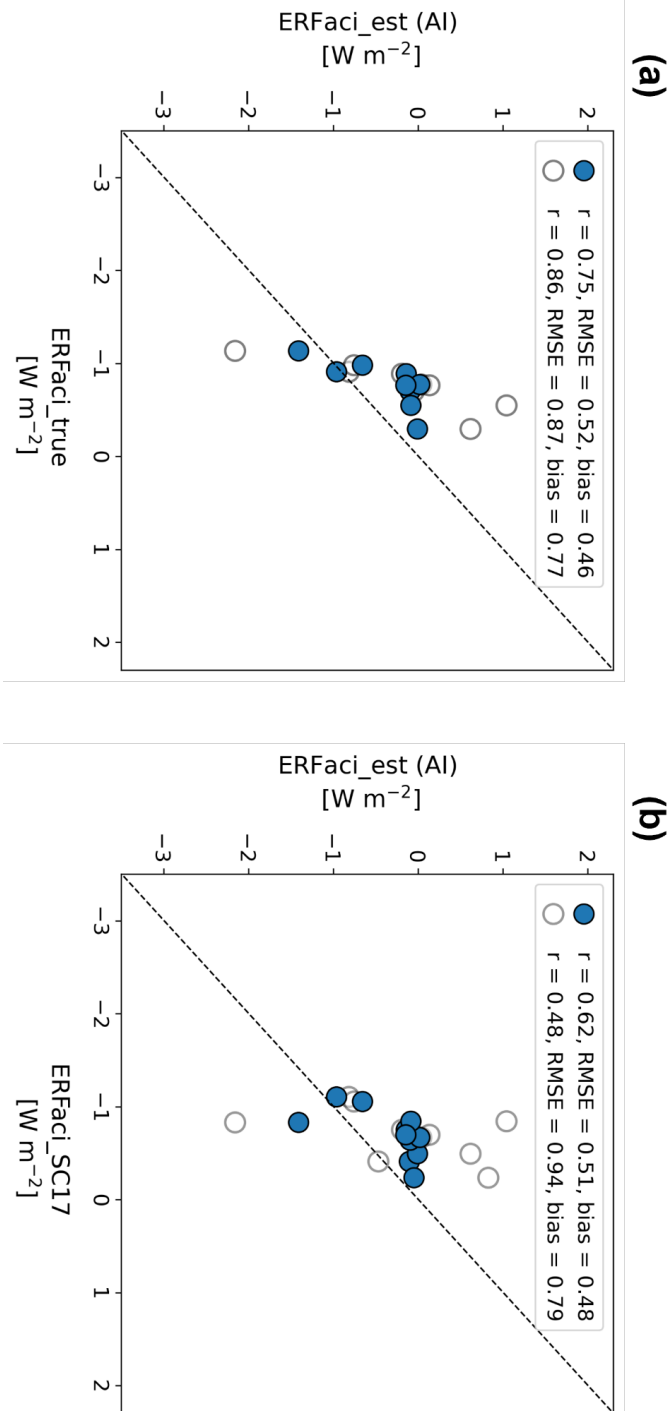
855 **Fig. A2.** Same as Fig. 2 but for AI. 9 models are used for changes in AI (Table A1).

856

857

858

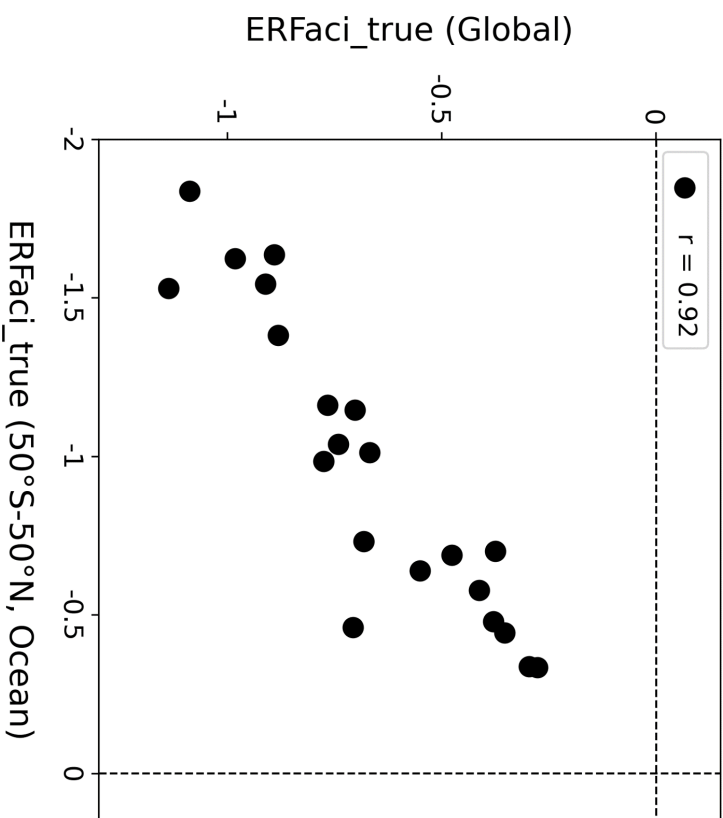
859



860
861 **Fig. A3.** Same as the first and last scatter plots in Fig. 3 but for the ERFaci_est estimated by AI instead of SO₄.

862

863



864
865
866 **Fig. A4.** CMIP6 estimates of ERFaci_true, averaged for the domain region (50°S to 50°N over ocean), and globally
867 averaged ERFaci_true values. Each black circle represents an individual model's estimate, with the correlation coefficient
868 (r) indicated in the upper left corner:



869 **Table A1.** CMIP6 models used in the analysis.

	Model	$\Delta\ln(\text{SO}_2)$	$\Delta\ln(\text{Al})$	ERFaci_true	ERFaci_SC17	ERFaci_est (SO ₂)	ERFaci_est (Al)	GOOD HIST index
1	ACCESS-CM2			0	0			0.323
2	ACCESS-ESM1-5			0	0			0.184
3	AWI-CM-1-1-MR				0			0.074
4	AWI-ESM-1-1-LR				0			0.141
5	BCC-CSM2-MR				0			0.319
6	BCC-ESM1	0		0	0	0		0.448
7	CAMS-CSM1-0				0			0.268
8	CanESM5			0	0			0.169
9	CanESM5-1				0			0.248
10	CanESM5-CanOE				0			0.306
11	CAS-ESM2-0				0			0.366
12	CESM2			0	0			0.147
13	CESM2-FV2				0			0.288
14	CESM2-WACCM				0	0		0.104
15	CESM2-WACCM-FV2				0			0.372
16	CIESM				0			0.212
17	CMCC-CM2-SR5				0			0.173
18	CMCC-ESM2				0			0.165
19	CNRM-CM6-1			0	0			0.029
20	CNRM-CM6-1-HR				0			0.014
21	CNRM-ESM2-1	0		0	0	0	0	0.191
22	E3SM-1-0				0			0.289
23	E3SM-2-0				0			0.749
24	EC-Earth3			0	0			0.136
25	EC-Earth3-AerChem	0	0	0	0	0	0	0.362
26	EC-Earth3-CC				0			0.503
27	EC-Earth3-Veg				0			0.153
28	EC-Earth3-Veg-LR				0			0.127
29	FGOALS-f3-L				0			0.115
30	FIO-ESM-2-0				0			0.256
31	GFDL-CM4	0		0	0	0		0.242
32	GFDL-ESM4	0	0	0	0	0	0	0.43
33	GISS-E2-1-G			0	0			0.347
34	GISS-E2-1-H				0			0.115
35	GISS-E2-2-G				0			0.272
36	GISS-E2-2-H				0			0.115
37	HadGEM3-GC31-LL	0	0	0	0	0	0	0.191
38	HadGEM3-GC31-MM				0			0.284
39	ICON-ESM-LR				0			0.287
40	INM-CM4-8				0			0.134
41	INM-CM5-0				0			0.201
42	IPSL-CM5A2-INCA				0			0.293
43	IPSL-CM6A-LR			0	0		0	0.157
44	IPSL-CM6A-LR-INCA	0		0				0.081
45	KACE-1-0-G				0			0.147
46	KIOST-ESM				0			0.15
47	MIROC6	0	0	0	0	0	0	0.327
48	MIROC-ES2L				0	0		0.296
49	MPI-ESM1-2-HR				0			0.15
50	MPI-ESM1-2-LR				0			0.072
51	MPI-ESM1-2-HAM	0	0	0	0	0	0	0.507
52	MRI-ESM2-0	0	0	0	0	0	0	0.329
53	NESM3				0			0.216
54	NorCPM1				0			0.17
55	NorESM2-LM	0	0	0	0	0	0	0.455
56	NorESM2-MM	0	0	0	0	0	0	0.366
57	SAM0-UNICON				0			0.362
58	TaiESM1				0			0.417
59	UKESM1-0-LL	0	0	0	0	0	0	0.325
60	UKESM1-1-LL				0			0.098

870